Evidence for novel transient clusters of cholinergic ganglion cells in the neonatal mouse retina

Jean de Montigny[1], Vidhyasankar Krishnamoorthy[1*], Fernando Rozenblit[2,3*], Tim Gollisch[2,3], Evelyne Sernagor[1]

1. Biosciences Institute, Faculty of Medical Sciences, Newcastle University, UK
2. Department of Ophthalmology, University Medical Center Göttingen, 37073 Göttingen, Germany
3. Bernstein Center for Computational Neuroscience Göttingen, 37077 Göttingen, Germany

* Equal contribution to the study

Abstract

Waves of spontaneous activity sweep across the neonatal mouse retinal ganglion cell (RGC) layer, driven by directly interconnected cholinergic starburst amacrine cells (the only known retinal cholinergic cells) from postnatal day (P) 0-10, followed by waves driven by glutamatergic bipolar cells. We found transient clusters of cholinergic RGC-like cells around the optic disc during the period of cholinergic waves. They migrate towards the periphery between P2-9 and then they disappear. Pan-retinal multielectrode array recordings reveal that cholinergic wave origins follow a similar developmental center-to-periphery pattern. Electrical imaging unmasks hotspots of dipole electrical activity occurring in the vicinity of wave origins. We propose that these activity hotspots are sites for wave initiation and are related to the cholinergic cell clusters, reminiscent of activity in transient subplate neurons in the developing cortex, suggesting a universal hyper-excitability mechanism in developing CNS networks during the critical period for brain wiring.

Introduction

During development, neural wiring is refined through activity-dependent processes (Blankenship and Feller, 2010; Luhmann et al, 2016). Spontaneous activity emerges long before sensory experience is possible, displaying unique expression patterns in different CNS areas. In the visual system, this activity is manifested by waves of spikes spreading across the retinal ganglion cell (RGC) layer (Meister et al, 1991). Several studies have demonstrated that retinal waves guide the development of visual connectivity (Huberman et al, 2008; Assali et al, 2014).

The cellular mechanisms underlying wave generation change with development, indicated by profound changes in the wave spatiotemporal features (Maccione et al, 2014). In mouse, the drive for wave generation/propagation switches from gap junction communication (Stage-1, prenatal) to cholinergic neurotransmission originating in starburst amacrine cells (SACs) (Stage-2, late gestation to P9) (Feller et al, 1996). Control then switches to glutamatergic bipolar cells before waves disappear around eye opening (Stage-3, P10-13). During Stage-2, SACs make direct homotypic connections, leading to lateral activity propagation across their network (Zheng et al, 2004). Experimental (Zheng et al, 2006; Ford et al, 2012) and theoretical studies (Butts et al, 1999; Hennig et al, 2009; Matzakos-Karvouniari et al, 2019) suggest that SACs play a fundamental role in defining wave dynamics by driving both wave initiation and propagation. Active SACs impose a refractory period, creating boundaries for activity propagation and controlling wave frequency. However, wave properties are not static during the prolonged Stage-2 period, exhibiting a gradual increase in wave frequency and size, followed by substantial shrinkage from P7 (Maccione et al, 2014). This suggests that Stage-2 wave initiation and propagation mechanisms may be more complex than originally assumed. Here we report for the first time that cholinergic RGC-like cells are transiently present during Stage-2 waves, and we propose that these cells may act as wave pacemakers.

Results

We have followed the pan-retinal expression of cholinergic cells during Stage-2 waves (P2-10) using immunostaining for the acetylcholine synthesizing enzyme Choline Acetyl Transferase (ChAT). To our surprise, we found clusters of ChAT-expressing cells (Figure 1, green dots) in the RGC layer (marked with RGC-specific RBPMS, red) forming an annulus of tight clusters in the vicinity of the optic disc at P2. As development progresses, the annulus expands, reaching the retinal periphery around P6-7. The clusters then begin to disintegrate and completely disappear by P10, coinciding with the switch from Stage-2 to Stage-3 waves.

We quantified the clusters' eccentricity during development (Figure 1B,C). The most substantial expansion occurs between P3-5, with no further eccentric movement beyond P6.

Closer inspection of the clusters revealed that these ChAT-expressing cells co-express RBPMS (Figure 2A), suggesting that they may be large cholinergic RGCs co-existing with much smaller SACs in the RGC layer (Figure 2B), but completely absent from the INL where SACs are the only ChAT-expressing cells. These cluster cells also express vesicular acetylcholine transporter (VAChT) on their soma and short processes, suggesting the presence of cholinergic synaptic terminals (Figure 2C). SACs also express VAChT, but in the classical double lamina pattern in the inner plexiform layer (IPL), flanked by cell bodies on both sides. Finally, the cholinergic identity of the cluster cells is confirmed by Sox2 (Figure 2D), a transcription factor expressed throughout life in retinal cholinergic cells (Whitney et al., 2014).

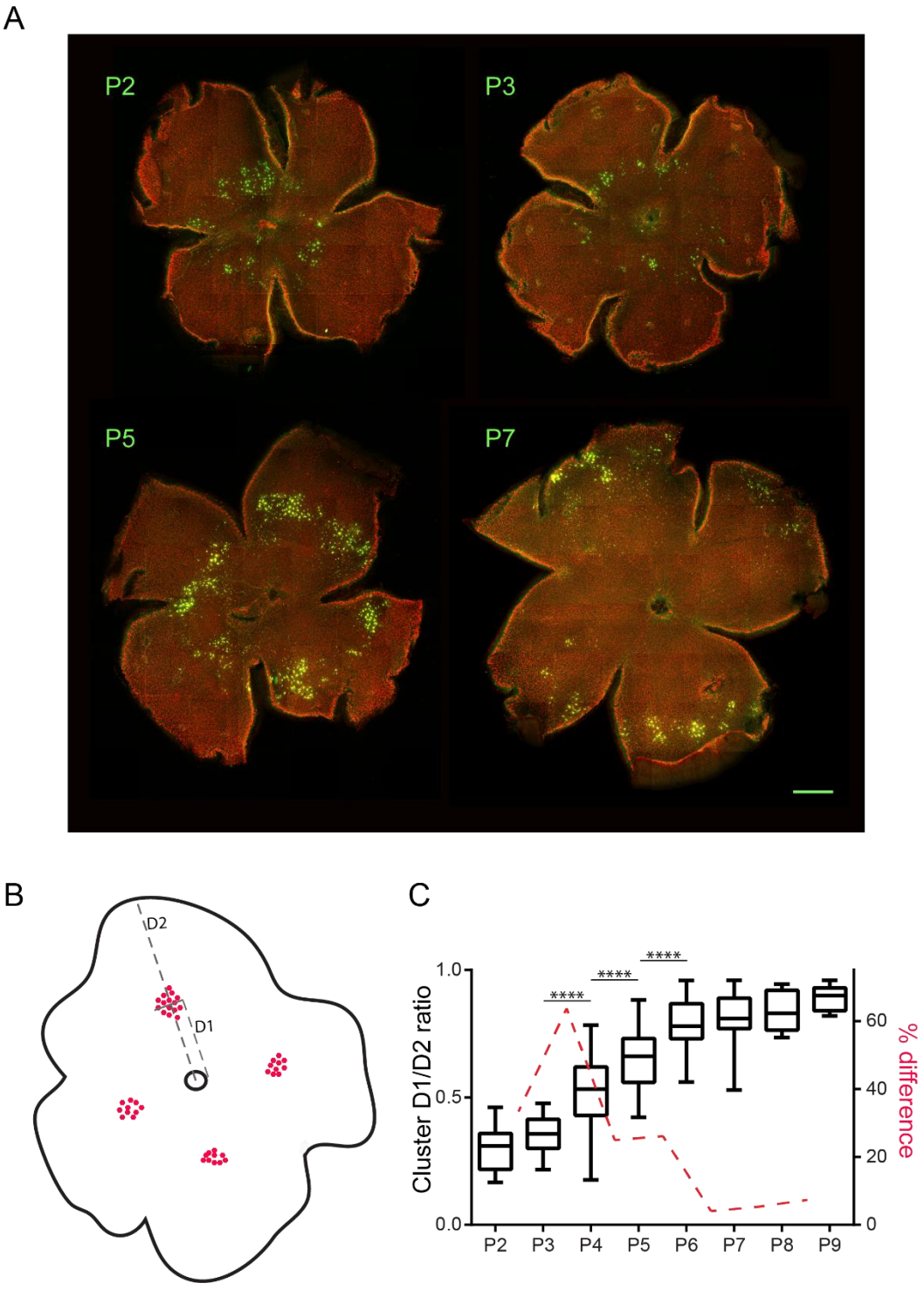

Figure 1: Retinal cholinergic cell clusters expansion from center to periphery during the first postnatal week. **A**: Mouse retinal wholemounts stained for ChAT (green) and RBPMS (red). Scale bar: 500 µm. **B**: Method for calculating the relative position of clusters between the optic disc (small black circle in the middle) and periphery. Cluster cells are represented by red dots. D1: distance from center of optic disc to center of cluster. D2: distance between center of cluster to periphery. **C**: Box plot showing developmental changes in D1/D2 ratio. Each box illustrates the median (horizontal line) and interquartile range, with minimum and maximum values (whiskers). Asterisks indicate significant changes between consecutive days (One-way ANOVA with post-hoc Tukey test). The red dotted line illustrates the percentage difference in values between consecutive days, showing peak difference between P3 and P4 and no further changes from P6 onwards.

The cholinergic clusters are present only during the period of Stage-2 waves, migrating from center to periphery between P2-7. We have previously shown that wave sizes also increase

from P2-6 (Maccione et al., 2014). These coincidental events made us wonder whether these clusters might be involved in wave generation. If so, we predict that wave origins would also migrate in an eccentric fashion during the first postnatal week. To address this possibility, we recorded waves between P2-13 using large-scale multielectrode arrays (MEAs) with 4,096 active electrodes spanning an area of 5.12x5.12 mm^2, large enough to cover the entire retinal surface at all ages (Figure 3). Wave origins (determined as the xy coordinates of the initial wave center of activity trajectory, see Maccione et al., 2014) were aligned with the image of the retina itself (Figure 3A, red dots, and B, green dots) and then classified as either central or peripheral (Figure 3A, see Methods). Figure 3C shows how the periphery/center ratios of wave origins change with development, expanding towards periphery between P2-7, with maximum change between P3-5, similar to the locations of the cholinergic clusters (Figure 1C). Once waves switch to Stage-3, the periphery-to-center ratio drops to 1 (or even lower), corroborating our previous findings that glutamatergic waves are small activity hotspots that tile the entire retina (Maccione et al., 2014).

To understand the possible functional involvement of these cellular clusters in wave generation, we used electrical imaging (Greschner et al, 2016; Zeck et al., 2011; Petrusca et al., 2007; Litke et al, 2004) (see Methods) to visualize wave-related electrical activity at high spatiotemporal resolution (Figure 4). Recordings were done on MEAs with either 81 μm or 42 μm electrode pitch, the latter providing higher spatial resolution. Although negative deflections smaller than the spike used for spike-triggered averaging (STA) were detected around most STA channels, presumably reflecting wave-related activity propagation (as in Channel 1782, Figure 4A and B), on some channels we could see conspicuous positive signals emerging simultaneously with the negative spike signal (Channel 1643, Figure 4A). These signals were significantly smaller (red asterisk) than the STA spikes (blue asterisk), but nevertheless easily distinct from baseline activity. Overall, when combining the activity footprint from all channels exhibiting such positive-negative "dipole" behavior (Figure 4C), we found that these areas form clusters in close proximity with wave origins (green dots in Figure 4C). However, when plotting all maximal projections, regardless of whether they have a positive deflection or not (Figure 4C, bottom row), the activity is more spread out over MEA channels, with less clear co-localization with the wave origins. The clustered layout of the dipole areas suggests that these signals may reflect activity originating from the cholinergic cell clusters.

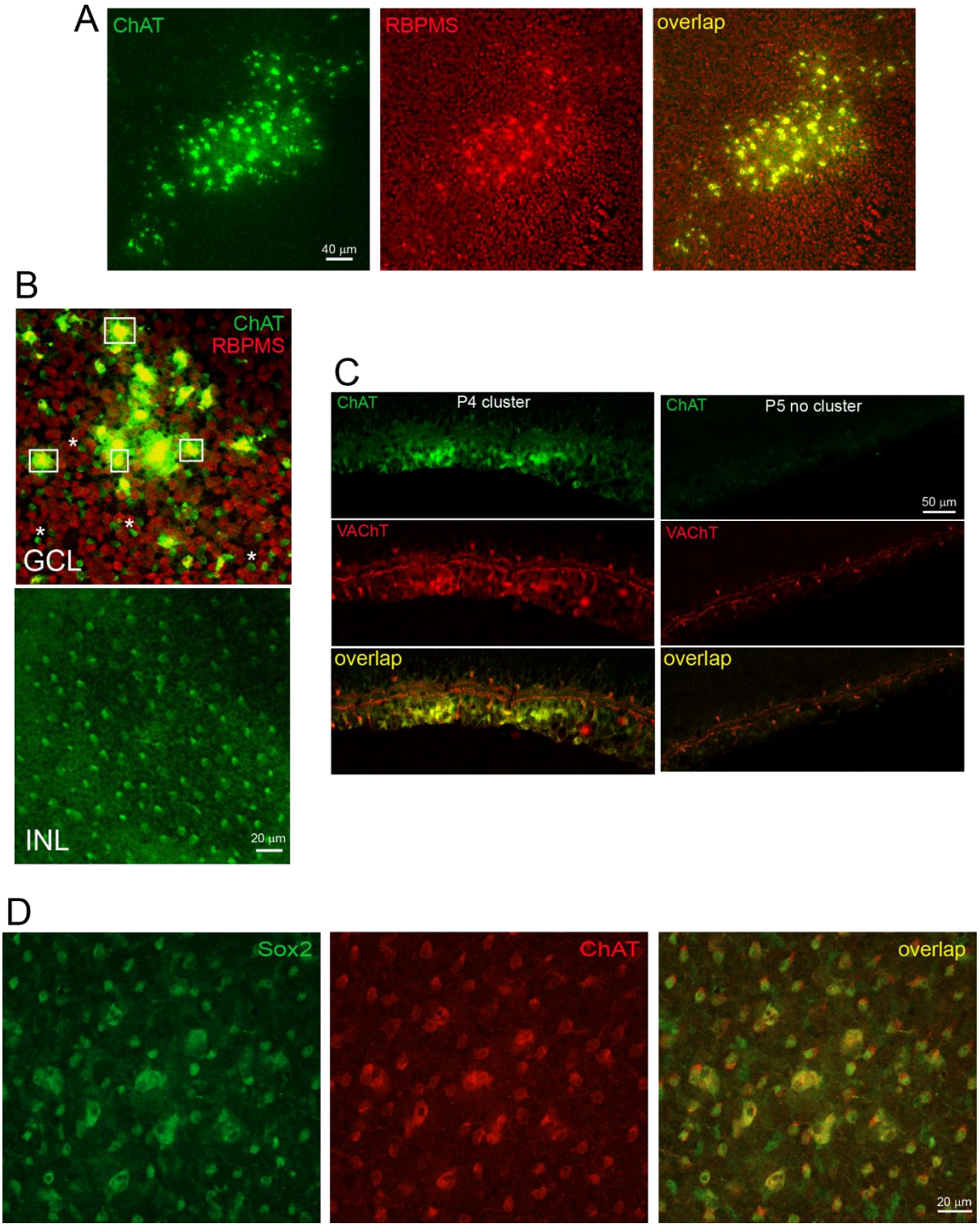

Figure 2: Cluster cells identified as cholinergic RGCs with immunolabeling. **A**: the images focus on one cluster (P5 retina), taken at the level of the RGC layer. Left panel: ChAT; middle panel: RBPMS; right panel: overlap of ChAT and RBPMS. All cluster cells co-express ChAT and RBPMS, suggesting they are cholinergic RGCs. **B**: P5 cluster viewed at the ganglion cell layer (GCL) level and at the INL level. Green: ChAT; red: RBPMS. At the GCL level, ChAT expressing clusters cells (examples marked within white boxes) co-exist with much smaller SACs (examples marked with asterisks). At the INL level, there are only SACs. **C**: Retinal sections showing ChAT (green) and VAChT (red) expression within a cluster (P4, left column) and in an area devoid of clusters (P5, right column). Cluster cells show strong VAChT expression. SACs express VAChT as well, exhibiting the typical double laminar expression in the IPL flanked by cell bodies in the INL and GCL (ChAT expression is weak in SACs at that age, increasing with development). In areas devoid of clusters, only the SAC expression

pattern can be seen. **D**: The large clusters cells and SACs both co-express Sox2 (green) and ChAT (red). There are some additional Sox2 expressing cells that do not express ChAT. These are presumably glial cells (Whitney et al., 2014).

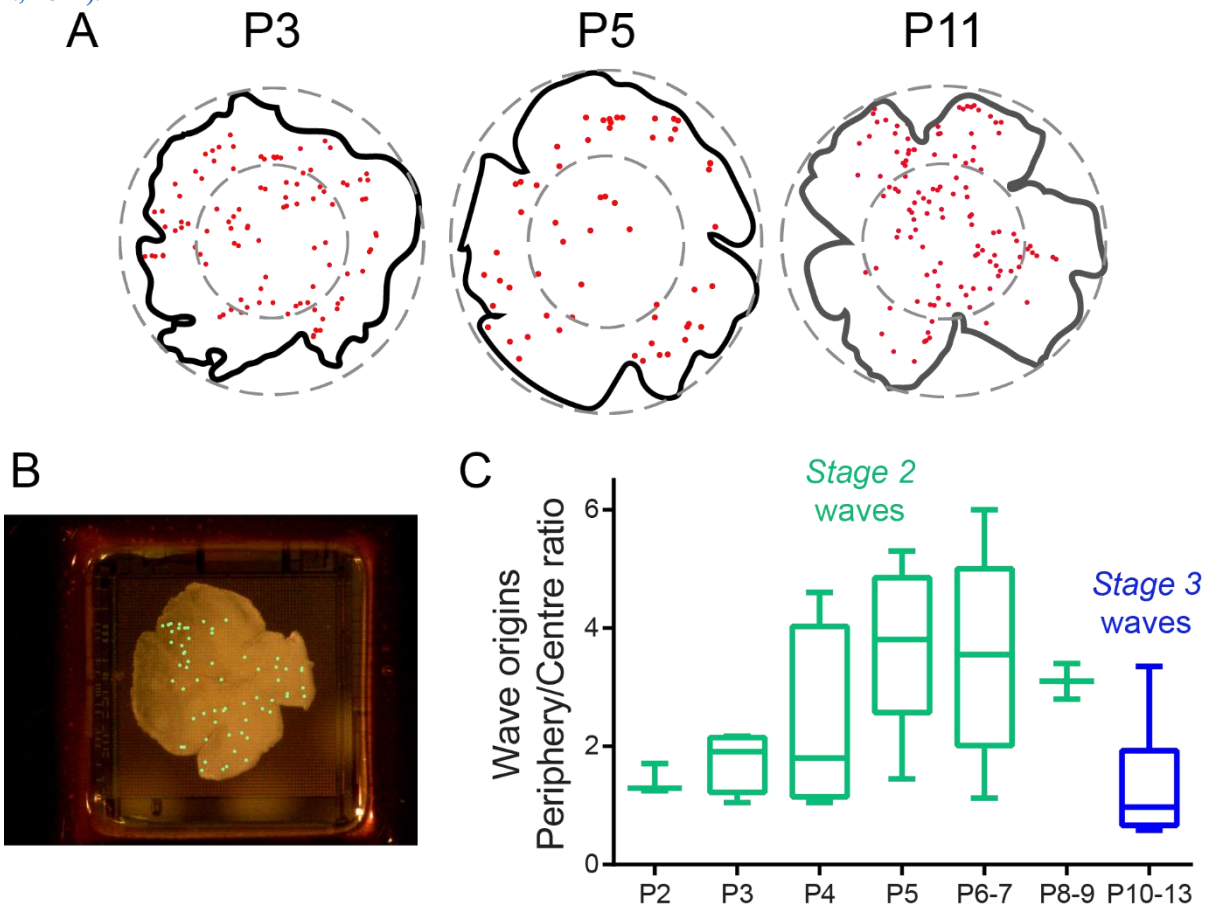

Figure 3: retinal waves and cluster cells. **A**: outlines of retinal wholemounts (black lines) photographed on the MEA immediately post recording (see **B** as well) overlaid with wave origins (red dots) detected during 30 minutes recording. Large grey dotted ellipses: encompass the whole retina. The smaller concentric ellipses (50% smaller than the large ones) indicate the central area. **B**: Photograph of a P4 retina on the MEA, taken at the end of the recording session. Wave origins (green dots) are overlaid on the photograph. **C**: boxplot illustrating the ratio between the number of wave origins in the periphery versus those in the central area. Wave origins expand from center to periphery between P2 and P5-6, similar to the clusters themselves (Figure 1C). Same boxplot conventions as for Figure 1C. Statistical analysis was not possible in this case due to the small numbers of values in each group (one ratio value per retina).

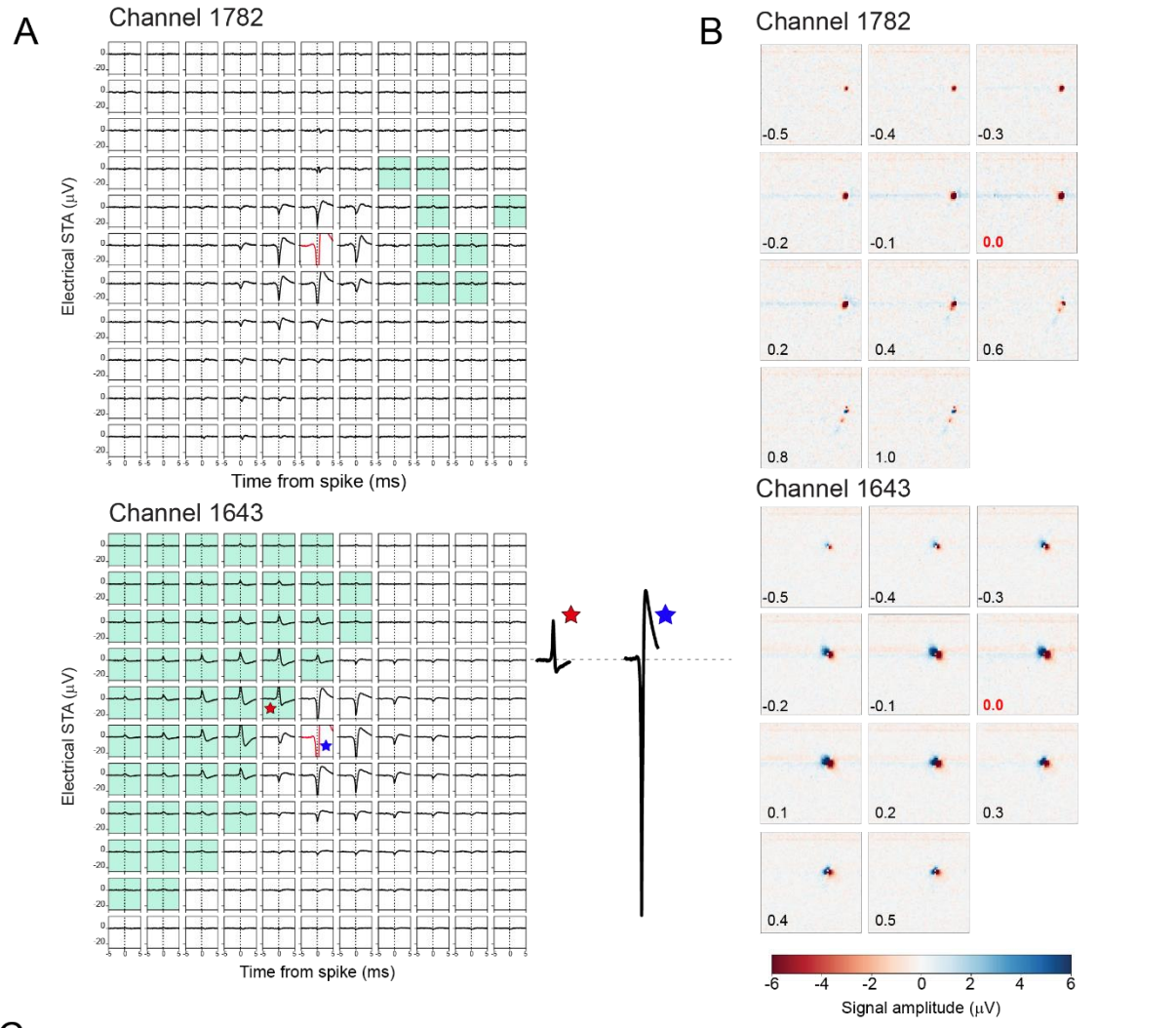

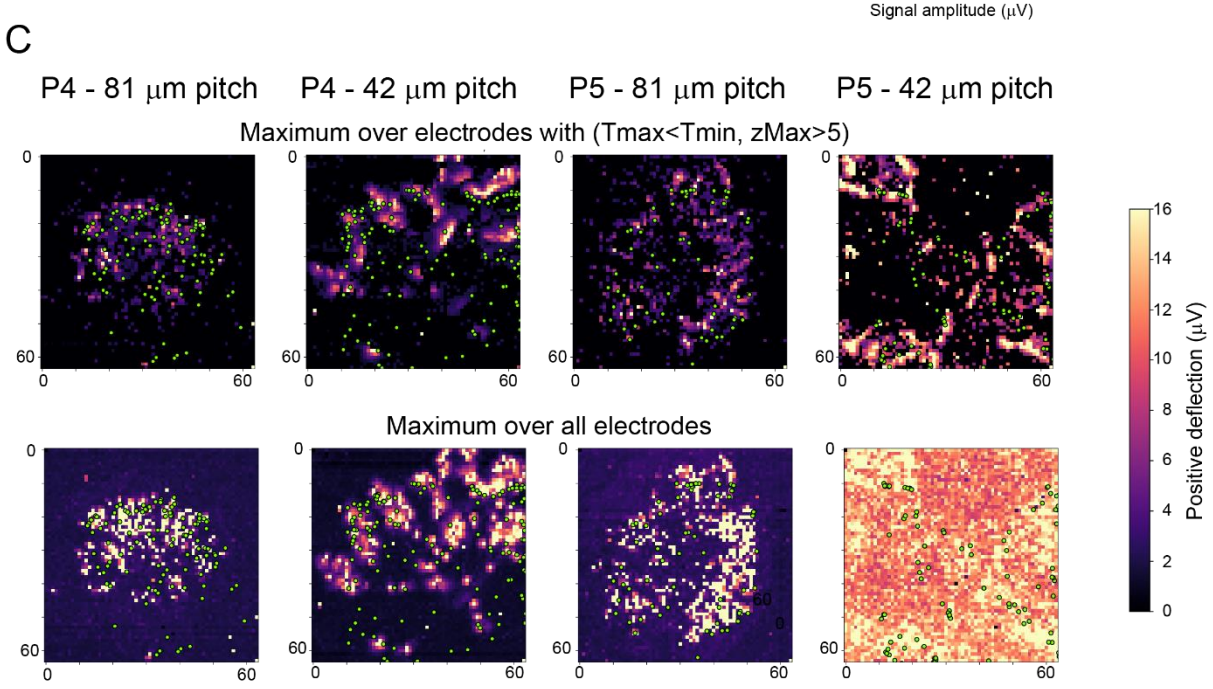

Figure 4: electrical imaging of retinal waves. **A**: STAs for two trigger channels showing signals averaged over -5 to +5 ms relative to spikes on the trigger channel (in red) for 11x11 surrounding recording channels. Recording

channels with dipole activity (with maximal positive deflections with z score>5 occurring before the maximal negative deflection, see Methods) are marked with the green mask. Channel 1643 has a marked area with dipole signals near the trigger channel. The single traces on the right side of the electrode grid show the full size of the spike on the trigger channel (blue asterisk) and maximal positive deflection (red asterisk), emphasizing the fact that the amplitude of the dipole signals is significantly smaller than spikes, suggesting that they may represent slow, graded potentials. (P4 retina, 60 min recording). **B**: Time-lapse images taken from movies of the averaged activity for both channels illustrated in **A**. The precise time of each image is indicated in the bottom left corner of each frame (in ms). Time 0.0 (time of the spikes used for STA) is indicated in red. For Channel 1643, clear dipole signals are seen from the earliest time frame (-0.5ms). Such signals are absent in Channel 1782. **C**: Maximal projections for signals with pre-STA spike signals with larger positive than negative deflections (top row) and for all maximal projections (bottom row) over the entire MEA. Maps are shown for two P4 and two P5 retinas, each with one example recorded on an array with 42 µm electrode pitch, and for another array with 81 µm pitch. Wave origins (green dots) are overlaid on the electrical signals.

Discussion

Adult RGCs come in many anatomical and functional varieties, but they all share one feature: they are glutamatergic neurons. Here we report for the first time that clusters of cholinergic RGC-like cells are transiently present in the mouse retina during the period of Stage-2 cholinergic waves. They appear near the optic disc at P2 and migrate to the periphery by P7 before disappearing at P10, coinciding with the switch to Stage-3 waves.

One plausible explanation that these cells have not been reported in previous studies is that they are sparse, and therefore may be easily missed if not visualized at pan-retinal level.

Several findings support the cholinergic RGC identity of these cells. Like SACs, their cholinergic signature is confirmed by ChAT, VAChT and Sox2 expression. But otherwise, they have features reminiscent of RGCs. Indeed, they express RBPMS, a selective RGC marker (Kwong et al, 2010; Rodriguez et al., 2014). Second, they are found only in the RGC layer, and not in the INL. Finally, they are much bigger than SACs, and they do not form a well-organized horizontal network spanning the entire retinal surface. It is unlikely that the cells physically migrate in the horizontal plane from the optic disc to the periphery over such a short period. It is also unlikely that they undergo programmed cell death like other RGCs (Young, 1984) because we could not detect apoptotic activity (with caspase3 immunostaining, data not shown) in these cells. Perhaps they die through microglial phagocytic engulfment (Cunningham et al., 2013). It is unlikely that they are undifferentiated cells because they do not express the transcription factor *Olig2* (data not shown), widely expressed in retinal progenitor cells (Hafler et al, 2012).

Our anatomical and physiological observations suggest that these cholinergic clusters may be responsible for the generation of Stage-2 waves. Indeed, using an MEA that is large enough to cover the entire retina, we found that wave initiation points move in a center-to-periphery fashion over a very similar time frame and pattern as the clusters. Waves expand in size up to P6 (Maccione et al, 2014), which could be due to their initiation points becoming gradually more peripheral. Unfortunately, due to shrinkage and repetitive handling of fixed retinas, we have not yet been able to reliably compare the locations of cholinergic clusters with wave origin points in corresponding living retinas.

Electrical imaging analysis demonstrates the presence of activity clusters characterized by simultaneous positive and negative small signals in proximity with wave origins, suggesting that these clusters may represent activity related to the cholinergic RGCs. We propose that

these cells act as hyper-excitable and hyper-connected hubs that trigger waves. Once generated, waves then travel across the retinal surface via the SAC network, as established in previous studies. Future studies are needed to reach a better understanding of the nature of the signals generated by these cells, and the extent of functional connectivity they make with SACs and other RGCs.

Although these cells have never been reported in the retina, developing cortical areas exhibit a transient population of subplate neurons that are highly active and synaptically connected to other developing neurons (Luhmann et al, 2018). The presence of transient, electrically active neurons during early development is thus not a new concept, suggesting a universal mechanism mediating hyper-excitability in developing CNS networks during the critical period for brain wiring.

Methods

Animals

All experimental procedures were approved by the UK Home Office, Animals (Scientific procedures) Act 1986.

Experiments were performed on neonatal (P2-13) C57bl/6 mice. All animals were killed by cervical dislocation followed by enucleation.

Immunostaining and imaging

For our anatomical studies, retinas were extracted from pups aged P2 (N=18 retinas), P3 (N=19), P4 (N=19), P5 (N=19), P6 (N=16), P7 (N=13), P8 (N=10), P9 (N=10), P10 (N=4) and P11 (N=4).

We have used the following antibodies:

Primary antibodies

ChAT (AB144P, goat polyclonal, Merck Millipore).

VAChT (PA5-77386, rabbit polyclonal, ThermoFisher Scientific).

RBPMS (1830-RBPMS, rabbit polyclonal, Phosphosolutions).

SOX2 (MAB2018, mouse monoclonal, R&D Systems).

Secondary antibodies

Donkey anti rabbit Alexa 568 (A10042, Invitrogen).

Donkey anti goat Dylight 488 (SA5-10086, ThermoFisher Scientific).

Rabbit anti mouse FITC (315-095-003, Jackson ImmunoResearch).

Retinal sections

Eyecups were prepared from mouse pups aged P2-P9, fixed for 45 min in 4% paraformaldehyde (PFA),), incubated in 30% sucrose in 0.1M phosphate buffer solution (PBS) for at least 12 hours, and then embedded in Optimal Cutting Temperature (OCT) cryo embedding compound and frozen at -20°C. Eyecups were sliced as 28µm thick sections using a cryostat (Model: OTF5000, Bright Instruments), washed with PBS to remove OCT, and incubated in blocking solution for 1 hour (5% secondary antibody host species serum with 0.5% Triton X-100 in PBS) prior to staining with antibodies.

Retinal sections were incubated with the primary antibody solution (0.5% Triton X-100 with VAChT (1:500 in PBS) and ChAT (1:500)) for 12 hours at 4°C. Sections were washed with PBS, followed by incubation with fluorescent secondary antibody solution (0.5% Triton X-100 with donkey anti rabbit Alexa 568 (1:500) and donkey anti goat Dylight 488 (1:500) in PBS) for 1 hour.

Finally, slices were washed with PBS and embedded with home-made OPTIClear refractive-index homogenisation solution. OPTIClear solution consists of 20% w/v N-methylglucamine, 25% w/v 2,2'-Thiodiethanol, 32% w/v Iohexol, pH 7-8. The solution is clear and colourless, with a refractive index of 1.47-1.48.

Sections were imaged using the Zeiss LSM 800 confocal microscope. Regions of interests were selected by using the ChAT staining in order to localise clusters.

Retinal wholemounts

Wholemount retinas were prepared from mouse pups aged P2-P11, flattened on nitrocellulose membrane filters and fixed for 45 min in 4% PFA. Retinas were then incubated in blocking solution (5% secondary antibody host species serum with 0.5% Triton X-100 in PBS) for 1 hour.

Two different immunostaining combinations were used:

- Primary antibodies: 0.5% Triton X-100 with RBPMS (1:500) and ChAT (1:500).
Secondary antibodies: 0.5% Triton X-100 with donkey anti rabbit Alexa 568 (1:500) and donkey anti goat Dylight 488 (1:500).
- Primary antibodies: 0.5% Triton X-100 with Sox2 (1:200) and ChAT antibody (1:500) in PBS as first antibody solution. 0.5% Triton X-100 with rabbit anti mouse FITC (1:500) and donkey anti goat Alexa 568 (1:500) in PBS as fluorescent secondary antibody solution.

Retinas were incubated with the primary antibody solution for 3 days at 4°C, then washed with PBS and incubated with the secondary antibody solution for 1 day at 4°C.

Finally, retinas were washed with PBS and embedded with OptiClear.

Zeiss AxioImager with Apotome processing and the Zeiss LSM 800 confocal microscope were used to image the retinas.

High-resolution images of the RGC layer down to the INL were obtained by subdividing retinal wholemounts into adjacent smaller images that were subsequently stitched back together to view the entire retinal surface. Regions of interests were selected by using the ChAT staining in order to localise clusters.

To compensate for variability in retinal thickness, several focus points were set across the retinal surface in order to keep sharp focus on the desired cell layer. Each individual picture was then acquired in all color channels at 20x magnification, and with 10% overlap between neighboring areas. This overlap is used to correctly align and stitch together all pictures using the Zen Pro software (Zeiss). Z-stacks of images at 40x magnification were acquired at regions of interest to visualize cells in 3D. Z-stacks consisted of images taken every 1 µm from the RGC layer to below the INL.

To calculate the relative position of the cell clusters between the optic disc and periphery, lines were traced and measured from the middle of the optic disc to the middle of a cluster (D1) and then from the same point in the cluster to the periphery of the retina (D2). D1/D2 represents the relative position of the clusters. One-way ANOVA was used on all 233 ratio values for all eight groups. Tukey post-hoc test was used to identify significant changes in cluster positions between consecutive developmental days.

Electrophysiology

MEA recordings

Retinas were isolated from mouse pups P2 (N=4 retinas), P3 (N=4), P4 (N=7), P5 (N=8), P6 (N=3), P7 (N=2), P8 (N=2), P9 (N=2), P10 (N=2), P11 (N=2), P12 (N=1), P13 (N=1). The isolated retina was placed, RGC layer facing down, onto the MEA and maintained stable by placing a small piece of polyester membrane filter (Sterlitech, Kent, WA, USA) on the retina followed by a home-made anchor. The retina was kept in constant darkness at 32°C with an in-

line heater (Warner Instruments, Hamden, CT, USA) and continuously perfused using a peristaltic pump (~1 ml/min) with artificial cerebrospinal fluid containing the following (in mM): 118 NaCl, 25 $NaHCO_3$, 1 NaH_2PO_4, 3 KCl, 1 $MgCl_2$, 2 $CaCl_2$, and 10 glucose, equilibrated with 95% O_2 and 5% CO_2. Retinas were allowed to settle for 2 hours before recording, allowing sufficient time for spontaneous activity to reach steady-state levels.

High resolution extracellular recordings of spontaneous waves were performed as described in details in Maccione et al. (2014), using the BioCam4096 platform with APS MEA chips type HD-MEA Stimulo (3Brain GmbH, Switzerland), providing 4096 square microelectrodes of 21 µm x 21 µm in size on an active area of 5.12 x 5.12 mm, with an electrode pitch of 81 µm. Two P5 and one P4 datasets were acquired with the MEA chip HD-MEA Arena (2.67x2.67mm active area, electrode pitch 42 µm).

Raw signals were visualized and recorded at 7 kHz sampling rate with BrainWaveX (3Brain GmbH, Switzerland). Each dataset consisted of 30 min of continuous recording of retinal waves. The datasets used for electrical imaging were acquired at 17.855 kHz for 30 or 60 min.

In the BioCam4096, samples of MEA signal are acquired row-wise by the amplifier. Individual samples consist of 64 columns and 64 rows and often show a small but measurable bias across rows of ca. 2-4 µV (1-2 ADC units). While such bias is negligible for most applications, it does degrade the quality of electrical images. Therefore, to reduce the bias before electrical imaging, the median value of each row was independently calculated and subtracted.

Retinas were photographed on the MEA at the end of the recording session to ensure we document the precise orientation of the retina with respect to the array of electrodes (Figure 3B).

Data processing and analysis

Burst and wave detection was done in Matlab (Mathworks) as described in Maccione et al. (2014). The xy coordinates of wave origins were then plotted on the MEA and overlaid with the retina itself in the appropriate orientation with respect to the MEA (green dots on Figure 3B). The outline of the retina was drawn for each preparation and overlaid with the array of wave origins (Figure 3A). The retinal outline was then delimited within an ellipse (outer ellipses, grey dotted lines, Figure 3A). A second, concentric ellipse with half the dimension of the outer ellipse was drawn to divide the retina into central and peripheral areas, and the number of wave origins (red dots, Figure 1A) was counted for both areas to calculate the periphery/center ratio of wave origins.

Electrical images were computed independently for each electrode by averaging the electrical activity in the MEA surrounding the time of spikes in that electrode (spike-triggered average). First, spikes were detected independently at each electrode with the default detection parameters of BrainWaveX (3Brain GmbH, Switzerland) (Maccione et al., 2014). To ignore electrodes without a good contact to the retina, only active electrodes – those with any noteworthy activity – were analyzed. Active electrodes were defined as having a normalised spike count

$$C(i) = \frac{N_i - \underset{j}{\text{median}}\left(N_j\right)}{1.4826 \times \underset{k}{\text{median}}\left(\left|N_k - \underset{j}{\text{median}}\left(N_j\right)\right|\right)} \geq 10,$$

where N stands for the spike count from an electrode. The denominator of C robustly estimates the standard deviation of spike counts using the median absolute deviation from the median (Quiroga et al., 2004; Donoho & Johnstone, 1994).

The electrical imaging itself proceeded as follows. For each active electrode, snippets of raw MEA signals were taken from -5 to +5 ms of the detected spike times. Only spikes appearing concomitantly with retinal waves were considered (wave onset and offset were determined by (i) detecting bursts on each electrode separately, and (ii) grouping bursts into waves based on temporal overlap and proximity, see Maccione et al., 2014 for further details). For the sampling rate of 17.855 kHz, a snippet consisted of 64 rows, 64 columns, and 180 sample points. Averaging the snippets thus led to a 64x64x180 movie $A_i(x,y,t)$ representing the typical electrical activity in the temporal vicinity of spikes from electrode i (Figure 4B). To remove noisy electrodes, electrical images whose negative peak of the spike had a half-peak width of less than 0.3 ms were discarded from the remaining analysis. To visualise the electrical activity, movies $A_i(x,y,t)$ were reduced to a map of negative deflections $S_i^{min}(x,y) = \min_t A_i$, positive deflections $S_i^{max}(x,y) = \max_t A_i$, and the times $T_i^{min}(x,y)$, $T_i^{max}(x,y)$ where such deflections occurred.

In some electrical images, a dipole activity was observed where positive deflections emerged simultaneously with the expected negative deflections of a spike. These positive lobes showed a strong positive deflection followed by a negative deflection (Figure 4A). To detect candidate regions with positive lobes, pixels (x,y) were selected when they had a significant positive deflection at a time $T_i^{max}(x,y)$ preceding the time of negative deflection $T_i^{min}(x,y)$ and not occurring later than 0.5 ms after the triggering spike. The latter condition helped to remove pixels exhibiting purely axonal propagation. Positive deflections were considered significant when their z-scored values

$$Z_i^{max}(x,y) = (S_i^{max}(x,y) - \mu)/\sigma \geq 5\,,$$

with $\sigma = 1.4826 \times \underset{i,x,y,t}{\text{median}} |A_i(x,y,t) - \mu|$ and $\mu = \underset{i,x,y,t}{\text{median}}\, A_i(x,y,t)$ (see C(i) above).

Defining a mask $W_i(x,y)$ as unity for such selected pixels with positive deflections (green background in Figure 4A) and zero everywhere else, the maximum projection (Figure 4C) over selected regions was given by $M_+(x,y) = \max_i W_i(x,y) S_i^{max}(x,y)$. The maximum over all electrodes, regardless of positive lobes, was given by $M_0(x,y) = \max_i S_i^{max}(x,y)$.

Acknowledgments

This work was supported by the Biotechnology and Biological Sciences Research Council (BBSRC, BH163322), Newcastle University Faculty of Medical Sciences and by the European Research Council (ERC) under the European Union's Horizon 2020 research and innovation programme (grant agreement number 724822).

JdM, VK and ES designed the experiments; JdM and VK performed the experiments; JdM and ES analyzed the experimental data; FR and TG designed and performed the electrical imaging analysis; ES and FR wrote the manuscript with input from the other authors.

References

Assali A, Gaspar P, Rebsam A (2014) Activity dependent mechanisms of visual map formation--from retinal waves to molecular regulators. Semin Cell Dev Biol 35:136-46. doi: 10.1016/j.semcdb.2014.08.008

Feller MB, Wellis DP, Stellwagen D, Werblin FS, Shatz CJ (1996) Requirement for cholinergic synaptic transmission in the propagation of spontaneous retinal waves. Science 272:1182-7. DOI: 10.1126/science.272.5265.1182

Blankenship AG, Feller MB (2010) Mechanisms underlying spontaneous patterned activity in developing neural circuits. Nat Rev Neurosci 11:18-29. doi: 10.1038/nrn2759.

Butts DA, Feller MB, Shatz CJ, Rokhsar DS (1999) Retinal waves are governed by collective network properties. J Neurosci 19:3580-93.

Cunningham CL, Martinez-Cerdeno V, Noctor SC (2013) Microglia regulate the number of neural precursor cells in the developing cerebral cortex. J Neurosci 33:4216–4233. doi: 10.1523/JNEUROSCI.3441-12.2013.

Donoho DL, Johnstone JM (1994) Ideal spatial adaptation by wavelet shrinkage. Biometrika 81:425-55.

Ford KJ, Félix AL, Feller MB (2012) Cellular mechanisms underlying spatiotemporal features of cholinergic retinal waves. J Neurosci 32:850-63. doi: 10.1523/JNEUROSCI.5309-12.2012

Greschner M, Heitman AK, Field GD, Li PH, Ahn D, Sher A, Litke AM, Chichilnisky EJ (2016) Identification of a Retinal Circuit for Recurrent Suppression Using Indirect Electrical Imaging. Curr Biol 26:1935-1942. doi: 10.1016/j.cub.2016.05.051

Hafler BP, Surzenko N, Beier KT, Punzo C, Trimarchi JM, Kong JH, Cepko CL (2012) Transcription factor Olig2 defines subpopulations of retinal progenitor cells biased toward specific cell fates. Proc Natl Acad Sci USA 109:7882-7. doi: 10.1073/pnas.1203138109

Hennig MH, Adams C, Willshaw D, Sernagor E (2009) Early-stage waves in the retinal network emerge close to a critical state transition between local and global functional connectivity. J Neurosci 29:1077-86. doi: 10.1523/JNEUROSCI.4880-08.2009

Huberman A, Feller MB, Chapman B et al. (2008) Mechanisms Underlying Development of Visual Maps and Receptive Fields Annu Rev Neurosci 31:479-509. doi: 10.1146/annurev.neuro.31.060407.125533

Kwong JM, Caprioli J, Piri N (2010) RNA binding protein with multiple splicing: a new marker for retinal ganglion cells. Invest Ophthalmol Vis Sci 51:1052-8. doi: 10.1167/iovs.09-4098

Litke AM, Bezayiff N, Chichilnisky EJ, Cunningham W, Dabrowski, W, Grillo AA, Grivich M, Grybos P, Hottowy P, Kachiguine S, Kalmar RS (2004) What does the eye tell the brain?: Development of a system for the large-scale recording of retinal output activity. IEEE Trans on Nuclear Sci 51: 1434-1440.

Luhmann HJ, Kirischuk S, Kilb W (2018) The superior function of the subplate in early neocortical development. Front Neuroanat 12:97. doi: 10.3389/fnana.2018.00097

Luhmann HJ, Sinning A, Yang JW, Reyes-Puerta V, Stüttgen MC, Kirischuk S, Kilb W (2016) Spontaneous neuronal activity in developing neocortical networks: from single cells to large-scale interactions. Front Neural Circuits 10:40. doi: 10.3389/fncir.2016.00040

Maccione A, Hennig MH, Gandolfo M, Muthmann O, van Coppenhagen J, Eglen SJ, Berdondini L, Sernagor E (2014) Following the ontogeny of retinal waves: pan-retinal recordings of population dynamics in the neonatal mouse. J Physiol 592:1545-63. doi: 10.1113/jphysiol.2013.262840

Matzakos-Karvouniari D, Gil L, Orendorff E, Marre O, Picaud S, Cessac B (2019). A biophysical model explains the spontaneous bursting behavior in the developing retina. Sci Rep 9:1859. doi: 10.1038/s41598-018-38299-4

Meister M, Wong RO, Baylor DA, Shatz CJ (1991) Synchronous bursts of action potentials in ganglion cells of the developing mammalian retina. Science 252:939-43.

Petrusca D, Grivich MI, Sher A, Field GD, Gauthier JL, Greschner M, Shlens J, Chichilnisky EJ, Litke AM (2007) Identification and characterization of a Y-like primate retinal ganglion cell type. J Neurosci 27:11019-27.

Quiroga RQ, Nadasdy Z, Ben-Shaul Y (2004) Unsupervised spike detection and sorting with wavelets and superparamagnetic clustering. Neural Comp16:1661-87.

Rodriguez AR, de Sevilla Müller LP, Brecha NC (2014) The RNA binding protein RBPMS is a selective marker of ganglion cells in the mammalian retina. J Comp Neurol 522:1411-43. doi: 10.1002/cne.23521

Whitney IE, Keeley PW, St John AJ, Kautzman AG, Kay JN, Reese BE (2014) Sox2 regulates cholinergic amacrine cell positioning and dendritic stratification in the retina. J Neurosci 34:10109-21. doi: 10.1523/JNEUROSCI.0415-14.2014

Young RW (1984) Cell death during differentiation of the retina in the mouse. J Comp Neurol 229:362-73.

Zeck G, Lambacher A, Fromherz P (2011) Axonal transmission in the retina introduces a small dispersion of relative timing in the ganglion cell population response. PLoS One 6: p.e20810. doi: 10.1371/journal.pone.0020810

Zheng JJ, Lee S, Zhou ZJ (2004) A developmental switch in the excitability and function of the starburst network in the mammalian retina. Neuron 44:851-64.

Zheng J, Lee S, Zhou ZJ (2006) A transient network of intrinsically bursting starburst cells underlies the generation of retinal waves. Nat Neurosci 9:363-71.